J. Fluid Mech. (2010), *vol.* 648, *pp.* 351–362. © Cambridge University Press 2010
doi:10.1017/S0022112009993909

A cloud of rigid fibres sedimenting in a viscous fluid

JOONTAEK PARK[1], BLOEN METZGER[2]†,
ÉLISABETH GUAZZELLI[2] AND JASON E. BUTLER[1]

[1]Department of Chemical Engineering, University of Florida, Gainesville, FL 32611, USA
[2]IUSTI-CNRS UMR 6596, Polytech-Marseille, Aix-Marseille Université (U1), Technopôle de Château-Gombert, 13453 Marseille cedex 13, France

(Received 2 October 2009; revised 7 December 2009; accepted 8 December 2009)

Experiments and numerical simulations have been performed to investigate the deformation and break-up of a cloud of rigid fibres falling under gravity through a viscous fluid in the absence of inertia and interfacial tension. The cloud of fibres is observed to evolve into a torus that subsequently becomes unstable and breaks up into secondary droplets which themselves deform into tori in a repeating cascade. This behaviour is similar to that of clouds of spherical particles, though the evolution of the cloud of fibres occurs more rapidly. The simulations, which use two different levels of approximation of the far-field hydrodynamic interactions, capture the evolution of the cloud and demonstrate that the coupling between the self-motion and hydrodynamically induced fluctuations are responsible for the faster break-up time of the cloud. The dynamics of the cloud are controlled by a single parameter which is related to the self-motion of the anisotropic particles. The experiments confirm these findings.

1. Introduction

The dispersion of swarms of particles occurs in natural processes of sedimentation of silt in rivers and on the continental shelf. The process has importance for the delivery of injected particles, such as catalysts, drugs and inoculated cells, into a bulk medium. Most of these natural phenomena or industrial applications involve anisotropic particles, but rod-like particles have received little attention as compared to spherical particles. In this paper, we consider the motion of a cloud of rigid fibres settling due to gravity in an otherwise pure liquid at low Reynolds number and in the absence of interfacial tension.

The deformation of clouds of spherical particles has been studied since Adachi, Kiriyama & Koshioka (1978) reported a complex evolution of the shape. A cloud having an initially spherical shape generally evolves into a torus that subsequently becomes unstable and breaks up into secondary droplets which deform themselves into tori in a repeating cascade. An extensive review has been presented by Machu *et al.* (2001). The cloud break-up was attributed to either inertia or to a perturbation on the shape of the initial cloud (Nitsche & Batchelor 1997; Schaflinger & Machu 1999; Machu *et al.* 2001; Bosse *et al.* 2005). Recent numerical simulations and experiments by Metzger, Nicolas & Guazzelli (2007) demonstrated that the break-up occurs even

---

† Email address for correspondence: bloen.metzger@polytech.univ-mrs.fr

in the complete absence of inertia and also without needing to perturb the initial shape.

Understanding the instability requires consideration of the discrete nature of the cloud of particles. Fluctuations arising from the multi-body character of the hydrodynamic interactions cause particles to depart from the closed toroidal circulation predicted by the continuum approach where the cloud is modelled as an effective medium of excess mass. Some of the particles may thus cross the cloud boundary and be carried into a downstream tail. Because the lost particles are those located in the toroidal circulation rim, this depletes the central region of the cloud and leads to the formation of a torus. The mechanism responsible for the further expansion of the torus remains unclear, but Metzger *et al.* (2007) described the break-up and showed a relationship with a change in the flow topology that occurs when the torus reaches a critical aspect ratio.

The present work investigates the deformation and break-up of a cloud of rigid fibres, focusing on the role of the particle anisotropy. Similar to clouds of spherical particles, we find that an initially spherical cloud of rigid fibres slowly evolves into a torus, which subsequently shatters into secondary droplets. However, the fluctuations in the velocities of the fibres originating from the particle anisotropy accelerates the break-up process as compared to clouds of spherical particles. We numerically identify the parameter that controls the break-up time and confirm it experimentally.

The simulations involved in this study are described in § 2. They have two different degrees of approximation for the far-field hydrodynamic interactions: the point-fibre, or 'fiblet' as we will designate it in the following, and slender-body dynamics. The former approximates the hydrodynamic interactions between fibres as those of point-particles and ignores short-range interactions (Mackaplow & Shaqfeh 1998; Saintillan, Shaqfeh & Darve 2006). The latter evaluates the long-range interaction at a higher level of approximation but, for simplicity, still does not consider the short-range interactions such as lubrication and excluded volume effects (Harlen, Sundararajakumar & Koch 1999; Butler & Shaqfeh 2002). The experiments are described in § 3 and compared with simulation results in § 4.

2. Simulation method

The initial clouds consist of N_0 rigid fibres, with length l and diameter d, distributed randomly in space and orientation inside a prescribed spherical volume of an unbounded fluid. The cloud settles under gravity through fluid that is Newtonian with viscosity μ. The fluid flow generated by the sedimenting particles satisfies the Stokes equations.

2.1. *Minimal description: the 'fiblet'*

This minimal model approximates the disturbance generated by fibres sedimenting in the fluid as that of point-particles. This approximation is sound for dilute suspensions where the distance between particles is large as compared to the length of the fibre, and the first-order term of the perturbation (Stokeslet) to the fluid velocity dominates. However, each particle rotates due to the velocity induced by the other sedimenting particles, and accordingly sediments through the fluid with a velocity that depends on its orientation.

Within this approximation, the translational velocity of particle α with position $\boldsymbol{r}_\alpha$ and orientation $\boldsymbol{p}_\alpha$ is the sum of its settling velocity $\boldsymbol{U}_s(\boldsymbol{p}_\alpha)$ when in isolation and of the disturbance velocity $\boldsymbol{u}(\boldsymbol{r}_\alpha)$ generated by the other fibres and evaluated at the centre of mass:

$$\dot{\boldsymbol{r}}_\alpha = \boldsymbol{U}_s(\boldsymbol{p}_\alpha) + \boldsymbol{u}_\alpha(\boldsymbol{r}_\alpha). \tag{2.1}$$

The settling velocity in a pure fluid is the product of the particle mobility, which is taken from the leading order of slender-body theory (Batchelor 1970; Cox 1970), and the buoyancy force acting upon the particle

$$\boldsymbol{U}_s(\boldsymbol{p}_\alpha) = \frac{\ln(2A)F}{4\pi\mu l}\left(\boldsymbol{I} + \boldsymbol{p}_\alpha\boldsymbol{p}_\alpha\right)\cdot\boldsymbol{e}_z, \tag{2.2}$$

where $A = l/d$ is the fibre aspect ratio, $\boldsymbol{I}$ is the identity tensor and F is the magnitude of the buoyancy force that acts along the z direction as designated by the unit vector $\boldsymbol{e}_z$. The disturbance velocity is the sum of point-forces as derived in the Appendix:

$$\boldsymbol{u}_\alpha(\boldsymbol{r}_\alpha) = \frac{F}{8\pi\mu}\sum_{\beta\neq\alpha}^{N_0}\left(\frac{\boldsymbol{I}}{|\boldsymbol{r}|} + \frac{\boldsymbol{r}\boldsymbol{r}}{|\boldsymbol{r}|^3}\right)\cdot\boldsymbol{e}_z, \tag{2.3}$$

where $\boldsymbol{r} = \boldsymbol{r}_\beta - \boldsymbol{r}_\alpha$ and $|\boldsymbol{r}|$ is the scalar length between the centres of particles α and β.

The rotational velocity of the fibres, also derived in the Appendix, is influenced only by the disturbances caused by the sedimentation of other fibres in the suspension,

$$\dot{\boldsymbol{p}}_\alpha = \frac{F}{8\pi\mu l}\left(\boldsymbol{I} - \boldsymbol{p}_\alpha\boldsymbol{p}_\alpha\right)\cdot\sum_{\beta\neq\alpha}^{N_0}\left[\frac{(\boldsymbol{r}\cdot\boldsymbol{p}_\alpha)\boldsymbol{I} - \boldsymbol{p}_\alpha\boldsymbol{r} - \boldsymbol{r}\boldsymbol{p}_\alpha}{|\boldsymbol{r}|^3} + \frac{3(\boldsymbol{r}\cdot\boldsymbol{p}_\alpha)\boldsymbol{r}\boldsymbol{r}}{|\boldsymbol{r}|^5}\right]\cdot\boldsymbol{e}_z. \tag{2.4}$$

Equations (2.1)–(2.4) represent the minimal model, which is referred to as the fiblet model because it is based upon point-particle interactions and includes the important aspect of particle rotation.

The only difference between (2.1) and the equation given for the motion of a cloud of point-particles by Metzger *et al.* (2007) is in the self-term $\boldsymbol{U}_s(\boldsymbol{p}_\alpha)$. Metzger *et al.* (2007) ignored the self-term when calculating the dynamics of a cloud of point-particles since it does not affect the relative motion of identical point-forces within a cloud and thus does not alter the overall dynamics of the cloud. For clouds of fiblets, the self-term depends on the particle orientation and generates a relative motion between the particles; therefore, this term must be retained to give even a qualitatively accurate solution.

Because the correct scaling of the length and time scales is not known *a priori*, we choose to scale the length and velocities by the initial radius of the cloud R_0 and the velocity $N_0F/5\pi\mu R_0$ of a spherical cloud of Stokeslets, respectively (Ekiel-Jeżewska, Metzger & Guazzelli 2006). The set of (2.2)–(2.4) becomes

$$\dot{\boldsymbol{r}}^*_\alpha = \frac{5c}{8N_0}\left(\boldsymbol{I} + \boldsymbol{p}_\alpha\boldsymbol{p}_\alpha\right)\cdot\boldsymbol{e}_z + \frac{5}{8N_0}\sum_{\beta\neq\alpha}^{N_0}\left(\frac{\boldsymbol{I}}{|\boldsymbol{r}^*|} + \frac{\boldsymbol{r}^*\boldsymbol{r}^*}{|\boldsymbol{r}^*|^3}\right)\cdot\boldsymbol{e}_z, \tag{2.5}$$

where $c = 2R_0\ln(2A)/l$ and * denotes dimensionless variables. Renormalizing (2.4) in the same manner gives

$$\dot{\boldsymbol{p}}^*_\alpha = \frac{5}{8N_0}\left(\boldsymbol{I} - \boldsymbol{p}_\alpha\boldsymbol{p}_\alpha\right)\cdot\sum_{\beta\neq\alpha}^{N_0}\left[\frac{(\boldsymbol{r}^*\cdot\boldsymbol{p}_\alpha)\boldsymbol{I} - \boldsymbol{p}_\alpha\boldsymbol{r}^* - \boldsymbol{r}^*\boldsymbol{p}_\alpha}{|\boldsymbol{r}^*|^3} + \frac{3(\boldsymbol{r}^*\cdot\boldsymbol{p}_\alpha)\boldsymbol{r}^*\boldsymbol{r}^*}{|\boldsymbol{r}^*|^5}\right]\cdot\boldsymbol{e}_z. \tag{2.6}$$

For a sufficiently large number of particles, the governing equations for the sedimentation velocity of fiblets reduces to the case of a cloud of Stokeslets as studied by Metzger *et al.* (2007). However, the self-term prevails over the hydrodynamic interactions between the particles as c becomes large relative to N_0. Consequently, different behaviours are expected for the cloud of fiblets, as compared to the cloud of Stokeslets.

Integration of positions and orientations was performed using a Bulirsch–Stoer method (Press *et al.* 1994). The method enforces a precision of 1×10^{-4} for the centre-of-mass positions over each time step. For each simulation, the time step was chosen such that an average particle sediments a distance of $l/20$ when in the initial spherical geometry with randomized positions and orientations.

2.2. *Higher level of description: slender-body dynamics*

Simulations are also performed with a higher level of description for the far-field hydrodynamic interactions. The code is similar to that presented by Butler & Shaqfeh (2002). The velocities of the N_0 fibres are related to the forces and torques acting on them through a mobility matrix $\mathscr{M}$,

$$\begin{vmatrix} \dot{\boldsymbol{r}} \\ \dot{\boldsymbol{p}} \end{vmatrix} = \mathscr{M} \cdot \begin{vmatrix} \boldsymbol{F} \\ \boldsymbol{T} \end{vmatrix}, \tag{2.7}$$

where $\dot{\boldsymbol{r}}$ and $\dot{\boldsymbol{p}}$ contain all components of the centre-of-mass and rotational velocities for all fibres, and $\boldsymbol{F}$ and $\boldsymbol{T}$ contain the components of force and torque acting on the fibres.

As constructed here, the mobility matrix contains the effects of far-field hydrodynamic interactions as distributed over the full length of both fibres, as opposed to the localization of the interactions at the centre of mass of the fibres as done for the fiblet calculation. The simulation scheme is the same as that described by Butler & Shaqfeh (2002), except the Oseen–Burgers tensor is used instead of the periodic Greens function of Hasimoto (1959) to enable simulations of swarms of concentrated particles in an infinite space. A fourth-order Runge–Kutta method advances the particle positions and orientations in time, with the time step determined by using an adaptive algorithm as described in Butler & Shaqfeh (2002).

This more accurate slender-body simulation requires more computational resources than the fiblet simulation; the maximum N_0 for the full simulation was limited to 1000 particles, whereas 4000 particles could be calculated using the fiblet algorithm. An aspect ratio of $A = 10$ is used for all simulations to match the experiments as well as to satisfy the slender-body limit.

Both codes were tested for convergence with regard to time step, and the limits (single particle, dilute and two-particle interactions) were tested with success. Note that for both simulations methods, interactions were not calculated between pairs of fibres when their separation distance was smaller than one fibre diameter. We found that including the cut-off distance for the hydrodynamic interaction is necessary, unlike in the case of Stokeslets used by Metzger *et al.* (2007). Other methods for controlling the singularities returned results similar to those when using this method, and the results were insensitive to the exact cut-off distance.

2.3. *Parameters describing the deformation*

Numerical simulations were performed with initially spherical clouds comprised of $500 \leqslant N_0 \leqslant 4000$ particles that were tracked over a typical time interval of $0 \leqslant t^* \leqslant 800$. To identify the time evolution of the deformation of a sedimenting cloud, we define some parameters such as the number of particles N that remain in the cloud, the sedimentation rate V of the cloud and the horizontal radius R and its rate of growth $\mathrm{d}R/\mathrm{d}t$. Because large variation exists from one run to the next for the same N_0, ten runs for different realizations of the initial particle positions were performed. This generates an ensemble of data over which to average the macroscopic quantities of the cloud as a function of time t^*. The mean values of parameters $\langle N\rangle$ and $\langle R\rangle$ are normalized by their initial values N_0 and R_0, respectively; the mean values of velocity parameters $\langle V\rangle$ and $\langle \mathrm{d}R/\mathrm{d}t\rangle$ are normalized by $N_0F/5\pi\mu R_0$. The dispersion of the data among runs is quantified by the standard deviation.

Particles are lost from the initially spherical cloud as it sediments through the fluid. The particles considered to belong to the cloud are those for which the vertical position from the centre of mass of the cloud is $\leqslant R_0$. This yields a definition for the particles inside the cloud $N^*(t^*)$ and, by averaging the individual velocities of these particles, the cloud velocity $V^*(t^*)$. The horizontal radius of the cloud $R^*(t^*)$ is calculated by dividing the cloud into four quadrants, measuring the maximum distance in the direction perpendicular to gravity of a particle from the centre of mass of the cloud, and averaging over the four values. Though alternatives can be proposed for quantifying the cloud radii, this option provides a method that is similar to that used for the experiments.

3. Experimental techniques

The experimental set-up and techniques are similar to those used by Metzger *et al.* (2007) where further detail can be found. The vessel has a width of 9.8 cm, a depth of 4cm, and a filled height of 100 cm. The rigid fibres are made of copper with a dimension of $l = 0.127 \pm 0.013$ cm and $d = 0.0149 \pm 0.0020$ cm, and density $\rho_p = 8.97 \pm 0.03$ g cm^{-3}. For these fibres, the aspect ratio is $A \approx 8.5$. The fluid is a mixture of 50 % by volume Ucon oil supplied by Chempoint and 50 % distilled water, and has a density $\rho = 1.079 \pm 0.19$ g cm^{-3} and a dynamic viscosity $\mu = 2170 \pm 60$ cP. With this combination of fluid and fibres, the typical Reynolds number, as based upon the radius and sedimentation velocity of the cloud, is less than 10^{-2}.

The suspension of rigid fibres is prepared with a desired volume fraction ϕ in a small beaker. Clouds are produced by injecting a given volume of suspension at the top of the filled container using a syringe. The shape of evolution of the clouds is recorded with a digital video camera CANON XM2 mounted on a vertical sliding rail. Homogeneous lighting is ensured by backlighting the vessel using a neon tube while placing a double layer of tracing paper to the back wall of the container.

The supplementary movies (available at journals.cambridge.org/FLM) are analysed with ImageJ (digital imaging software available at http://rsb.info.nih.gov/ij/). Each image is thresholded and the cloud contour is fitted with an ellipse. This provides the position of the centre of mass and the horizontal R dimension of the cloud. The instantaneous cloud velocity V is measured from two successive frames. The initial dimension R_0 and velocity V_0 of the experimental cloud are used to normalize the data in the same way as in the simulations. Statistics were obtained as in the numerical simulations by doing several runs (typically five).

4. Results and comparisons

As evident from the fiblet model (see § 2.1), the settling behaviour of a spherical cloud depends strongly on the value of c/N_0. For large c/N_0, the self-term overwhelms the hydrodynamic interactions between particles and the fibres behave as when in isolation. In the other limit of $c/N_0 = 0$, the governing equations become identical to the case of a cloud of Stokeslets and the cloud behaves accordingly. We are interested in the regime where $c/N_0 < 1$ so that the hydrodynamic interactions prevail, yet the values of c are large enough for the self-term, and thus the anisotropy of the particles, to have a substantial influence on the evolution of the cloud.

Figure 1 illustrates the typical evolution of a cloud of fibres versus time in the experiments and the fiblet simulations which have been undertaken in the range $0.01 \leqslant c/N_0 \leqslant 0.1$ (see supplementary movies). This evolution closely resembles that of a falling cloud of spheres which has been successfully modelled by Stokeslets (Metzger *et al.* 2007). The initially spherical cloud begins to lose particles at a slow, steady rate while falling through the viscous fluid. The cloud continuously expands in the direction perpendicular to gravity and transitions into a toroidal shape. This torus eventually fractures into multiple droplets of particles (usually into more than two droplets in contrast with a cloud of spheres which mostly breaks up into two). Each of these droplets can destabilize again in a repeating cascade if the cloud contains a large enough number of particles.

In figure 2, the mean value of the break-up time, $\langle t_b^* \rangle$, estimated as the normalized time for which the torus starts to bend before breaking, is plotted versus c and c/N_0. The major trend seen in figure 2(*a*) is that $\langle t_b^* \rangle$ declines with increasing c, i.e. with increasing prominence of the self-term. The two simulation methods give similar results. As found for the falling cloud of spheres (or Stokeslets, i.e. $c = 0$), $\langle t_b^* \rangle$ increases with N_0. By plotting $\langle t_b^* \rangle$ versus c/N_0 in figure 2(*b*), the numerical data corresponding to both simulation methods collapse onto the same curve. Excellent quantitative agreement is found between simulations and experiments.

In this latter figure, in addition to the present experimental data obtained for $A \approx 8.5$, we have also included experimental data from figure 3(*b*) of Metzger *et al.* (2007). These data, obtained for $A = 1$ and for $c/N_0 \approx 0.01$, also collapse onto the master curve. These results from two different values of A strengthen the finding from the simulations that the break-up time depends solely on c/N_0. Additional tests with moderately higher aspect ratios, such as $A \approx 30$, are feasible, but would reveal little as the fundamental parameter c has a weak logarithmic dependence on A; problems caused by the bending of our fibres at very large aspect ratios unfortunately prevent experiments on a wider range of parameters. Note that for the c/N_0 examined in the experiments, the volume fraction of the cloud ranges from 1 to 10 %.

The decrease of the break-up time with increasing c is linked to the faster growth of the horizontal radius of the cloud, R^*, with increasing c, i.e. with increasing importance of the self-term. This is evidenced in figure 3(*a*) by comparing the simulation results for $c = 40$ and 80. Good agreement is found between experiments and simulation results having similar c/N_0 despite large variations among runs.

Another distinct feature of falling clouds of rigid fibres, as compared to clouds of spheres, is seen in the evolution at the start of sedimentation; see figure 3(*b*). The initial sedimentation rate $\langle V_0^* \rangle$ is slightly faster than that of a cloud of Stokeslets with the same R_0 and a sufficiently large number of N_0 owing to the contribution of the self-term. At short times after the start of sedimentation, $\langle V^* \rangle$ rapidly increases to a maximum value (which is more pronounced for larger c) then decreases continuously, while $\langle V^* \rangle$ of the Stokeslet cloud only declines (Metzger *et al.* 2007). This initial increase in $\langle V^* \rangle$ is caused by a combination of the change in orientation distribution and a compaction of the cloud at short times as reflected by the small initial decrease in $\langle R^* \rangle$. This initial feature does not seem to be observed in the experiments. While there

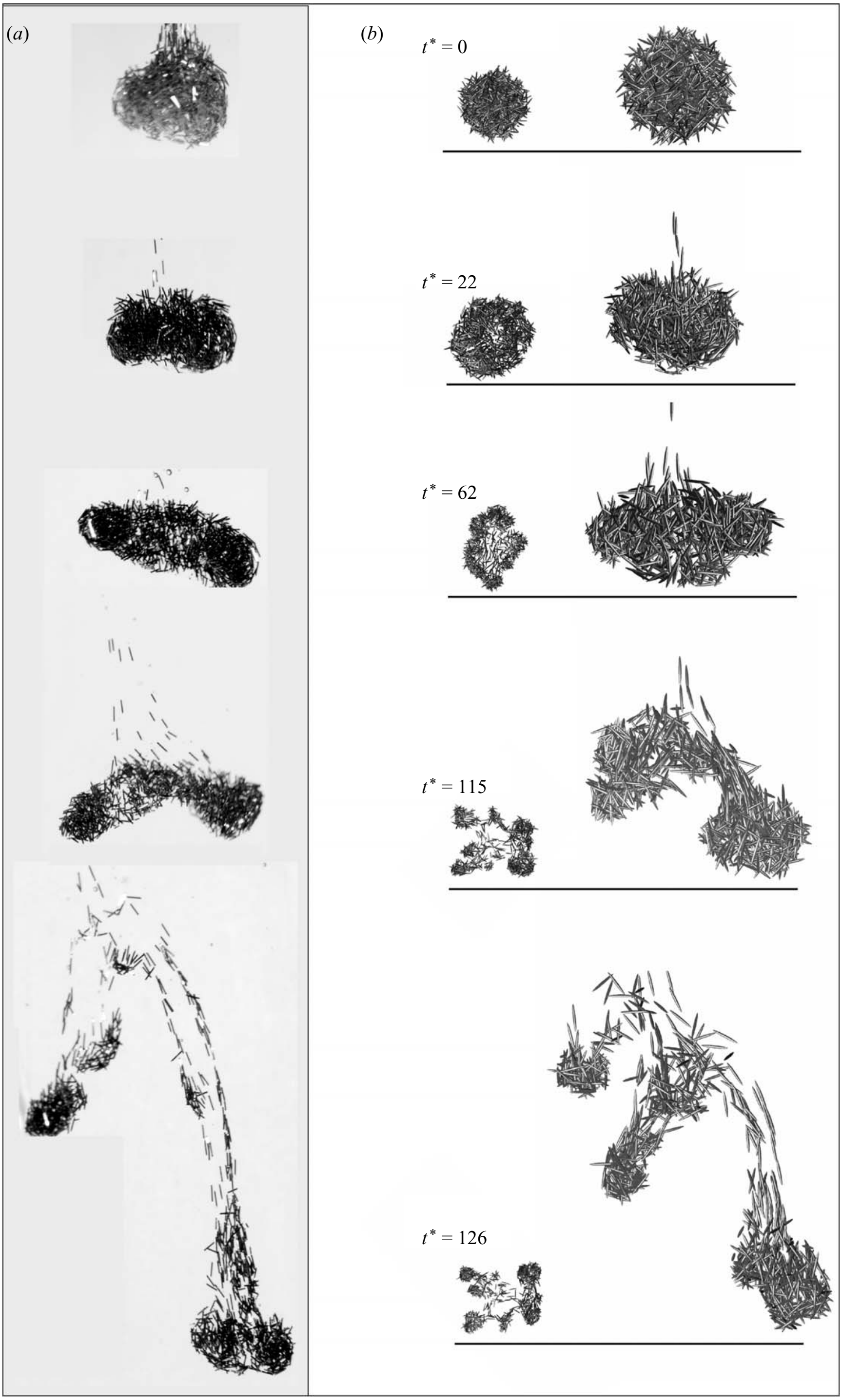

FIGURE 1. Typical evolution of a cloud of rigid fibres. (*a*) Experiment with $N_0 \approx 1000$ and $c \approx 30$, which corresponds to a cloud volume fraction of 5 %. (*b*) The fiblet algorithm for $c = 40$ and $N_0 = 1000$. The side views are accompanied by bottom views on the small side pictures. The complete dynamics coming from different runs are shown in the supplementary movies.

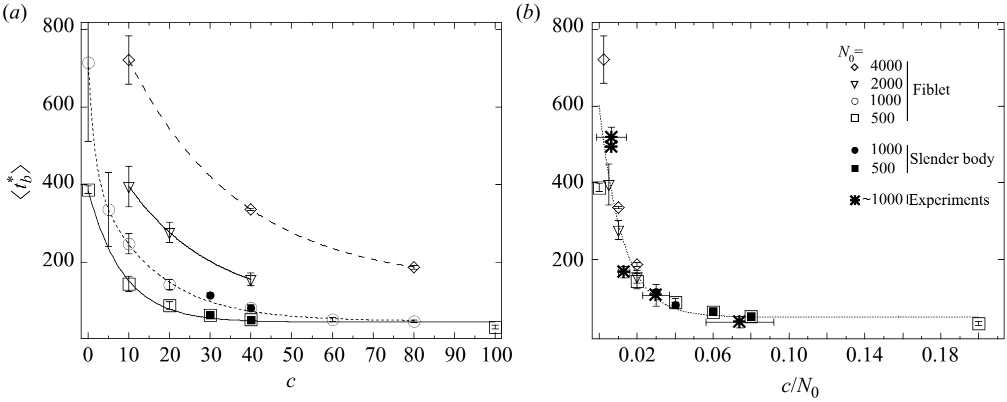

FIGURE 2. Mean value of the break-up time, $\langle t_b^* \rangle$, vs. (a) c and (b) c/N_0. The error bars correspond to the variance between runs.

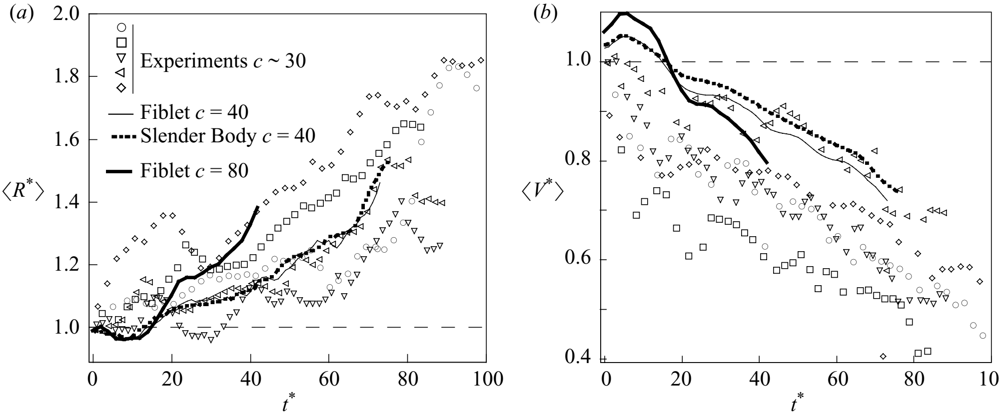

FIGURE 3. Simulation results for the time evolution of (a) the mean horizontal radius of the cloud, $\langle R^* \rangle$, and (b) the cloud settling velocity, $\langle V^* \rangle$ for clouds having $N_0 = 1000$. The two figures also show the values of R^* and V^* for five individual experimental runs. The dashed lines are guidelines for comparison with the initial radius and velocity of the cloud.

is a considerable variation among runs, the further decrease of $\langle V^* \rangle$ is comparable in experiments and simulations having the same c/N_0.

The influence of the self-term on the rate of growth of the cloud, $\langle \mathrm{d}R^*/\mathrm{d}t^* \rangle$, is examined with more detail in figure 4 for the fiblet simulations. Figure 4(a) shows the evolution of $\langle \mathrm{d}R^*/\mathrm{d}t^* \rangle$ for $c = 10$ according to each contribution: the self-term and the hydrodynamic term in (2.5). Comparing each contribution, the hydrodynamic term controls $\langle \mathrm{d}R^*/\mathrm{d}t^* \rangle$ and the self-term seems to contribute only relatively small fluctuations. However, even being small, the self-term contribution is fundamental to the accelerated break-up of clouds of fibres as compared to clouds of spheres. The value of $\langle \mathrm{d}R^*/\mathrm{d}t^* \rangle$ fluctuates between negative and positive values as the fibres tumble within the cloud, but the overall value becomes positive (indicating an expansion of the horizontal radius) and increases rapidly just prior to break-up of the unstable torus in stark contrast with the situation shown in figure 4(b) in which the self-term has been removed as in a Stokeslet cloud ($c = 0$).

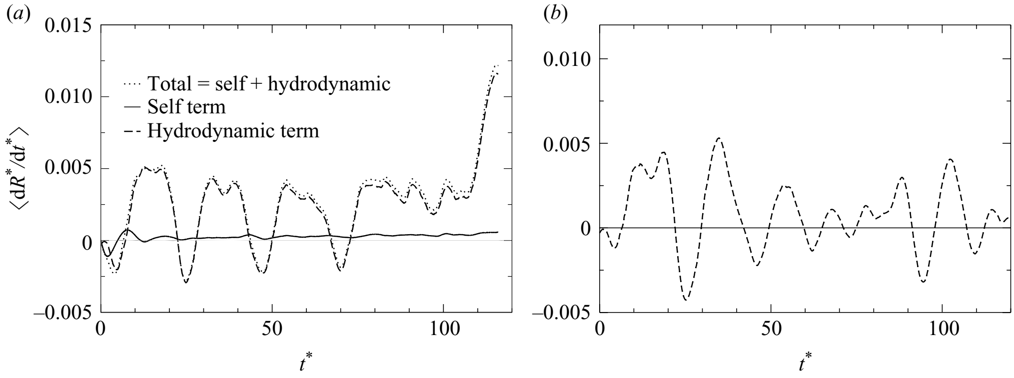

FIGURE 4. Time evolution of $\langle \mathrm{d}R^*/\mathrm{d}t^* \rangle$ resulted from fiblet simulations with $N_0 = 500$ and (*a*) $c = 10$ and (*b*) $c = 0$. Results are shown according to contributions from (2.5).

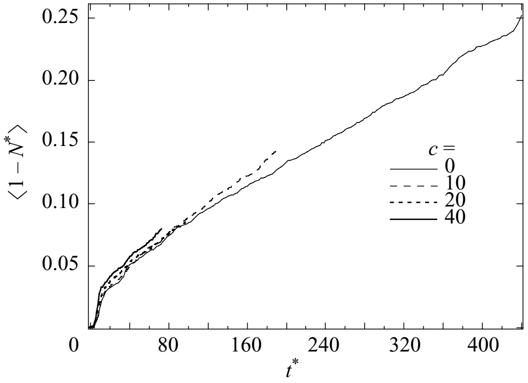

FIGURE 5. Fraction, $1 - N^*$, of particles that have leaked away from the cloud vs. time t^* for fiblet simulations having $N_0 = 1000$.

Finally, we have examined the fraction, $1 - N^*$, of particles that have leaked away from the cloud versus time t^* in figure 5 for the fiblet simulations. Clearly, the rate of leakage does not vary with c. This shows that the time evolution of the fraction of particles escaping from a cloud of fibres follows the same behaviour as that found from a cloud of spheres which has been examined in detail by Nitsche & Batchelor (1997) and Metzger *et al.* (2007).

5. Conclusions

We have studied the sedimentation of a cloud of rigid fibres through numerical simulations and experiments. The general evolution of the cloud deformation is found to be qualitatively similar to that of a cloud of spheres. However, quantitative differences in the time evolution are observed. For example, the particle anisotropy accelerates the expansion of the cloud and leads to a faster break-up.

Two simulations having different levels of approximation for the far-field hydrodynamic interactions, the fiblet and the slender-body, are performed and found to give similar results. These simulations demonstrate that the dynamics of the cloud are controlled by a single parameter, c/N_0, which is related to the self-term contribution to the motion of the anisotropic particles. The experiments confirm these findings.

Note also that the fiblet simulation, which contains the minimal physics, captures the cloud dynamics extremely well. The success of this minimal description indicates that (i) the first-order term of the far-field hydrodynamic interactions between the particles is sufficient and (ii) including the short-range interactions is not necessary for the range of volume fractions used in the experiments. It is indeed interesting to note that this later range extends from the dilute to the semi-dilute regime as $0.16 \lesssim n(l/2)^3 \lesssim 1.6$ where n is the number of particles per unit volume.

This work was supported by the National Science Foundation through a CAREER Award (CTS-0348205). Visits were supported by the Partner University Fund on ‘particulate flows’ and by Aix-Marseille Université (U1) visiting professorships.

Supplementary movies are available at journals.cambridge.org/FLM.

Appendix. Formulation of the fiblet approximation

Slender-body theory (Moran 1963; Batchelor 1970; Cox 1970) is assumed to describe the motions of the high aspect fibres sedimenting in the Newtonian fluid under Stokes conditions, or vanishing Reynolds number. At the leading order of approximation within the slender-body equations, the centre-of-mass velocity of a fibre α is

$$\dot{\boldsymbol{r}}_\alpha = \frac{\ln(2A)F}{4\pi\mu l}\left(\boldsymbol{I}+\boldsymbol{p}_\alpha\boldsymbol{p}_\alpha\right)\cdot\boldsymbol{e}_z + \frac{1}{l}\int_{-l/2}^{l/2}\boldsymbol{u}_\alpha\left(\boldsymbol{r}_\alpha+s_\alpha\boldsymbol{p}_\alpha\right)\mathrm{d}s_\alpha, \tag{A 1}$$

where $\boldsymbol{u}_\alpha(\boldsymbol{r}_\alpha + s_\alpha\boldsymbol{p}_\alpha)$ is the fluid velocity evaluated at position $\boldsymbol{r}_\alpha + s_\alpha\boldsymbol{p}_\alpha$ along the centreline of fibre α. The coordinate s_α is set such that $-l/2 \leqslant s_\alpha \leqslant l/2$ and $s_\alpha = 0$ at the centre of mass. The rotational velocity of the fibre α is

$$\dot{\boldsymbol{p}}_\alpha = \frac{12}{l^3}\left(\boldsymbol{I}-\boldsymbol{p}_\alpha\boldsymbol{p}_\alpha\right)\cdot\int_{-l/2}^{l/2}\boldsymbol{u}_\alpha\left(\boldsymbol{r}_\alpha+s_\alpha\boldsymbol{p}_\alpha\right)s_\alpha\,\mathrm{d}s_\alpha, \tag{A 2}$$

where the external torque on the fibre is zero.

In an otherwise quiescent fluid, the fluid velocity at a position on fibre α is generated by the sedimentation of the other fibres, labelled β, in the suspension. This velocity is calculated by summing the disturbance created by distributing Stokeslets along the centreline of each fibre β (Harlen *et al.* 1999; Butler & Shaqfeh 2002) as

$$\boldsymbol{u}_\alpha\left(\boldsymbol{r}_\alpha+s_\alpha\boldsymbol{p}_\alpha\right) = \sum_{\beta\neq\alpha}^{N_0}\int_{-l/2}^{l/2}\boldsymbol{J}\left(\boldsymbol{r}_\beta+s_\beta\boldsymbol{p}_\beta-\boldsymbol{r}_\alpha-s_\alpha\boldsymbol{p}_\alpha\right)\cdot\boldsymbol{f}\left(s_\beta\right)\mathrm{d}s_\beta, \tag{A 3}$$

where $\boldsymbol{J}$ is the Oseen–Burger tensor and $\boldsymbol{f}(s_\beta)$ is the line force density of Stokeslets on fibre β. The description of the dynamics is completed by specifying that the fibres are torque-free, $\int s_\beta \boldsymbol{f}_\beta(s_\beta)\,\mathrm{d}s_\beta = 0$, and acted on by a net buoyancy force, $\int \boldsymbol{f}_\beta(s_\beta)\,\mathrm{d}s_\beta = F\boldsymbol{e}_z$.

Equations (2.1)–(2.4) are developed by linearizing both the velocity on fibre α and the velocity generated by fibre β about their respective centres. For particles that are widely separated, the velocity variation along the length of the fibre varies little and can be approximated by two terms of the Taylor series about the centre of mass, $s_\alpha = 0$,

$$\boldsymbol{u}\left(\boldsymbol{r}_\alpha+s_\alpha\boldsymbol{p}_\alpha\right) \approx \boldsymbol{u}\left(\boldsymbol{r}_\alpha\right) + s_\alpha\left.\frac{\partial\boldsymbol{u}}{\partial s_\alpha}\right|_{\boldsymbol{r}_\alpha}. \tag{A 4}$$

Using this approximation gives

$$\dot{\boldsymbol{r}}_\alpha = \frac{\ln(2A)F}{4\pi\mu l}\left(\boldsymbol{I}+\boldsymbol{p}_\alpha\boldsymbol{p}_\alpha\right)\cdot\boldsymbol{e}_z + \boldsymbol{u}_\alpha\left(\boldsymbol{r}_\alpha\right) \tag{A 5}$$

and

$$\dot{\boldsymbol{p}}_\alpha = \left(\boldsymbol{I}-\boldsymbol{p}_\alpha\boldsymbol{p}_\alpha\right)\cdot\left.\frac{\partial\boldsymbol{u}}{\partial s_\alpha}\right|_{\boldsymbol{r}_\alpha}. \tag{A 6}$$

Likewise, the velocity disturbance at $\boldsymbol{r}_\alpha$ due to the force applied at point s_β on a fibre β is linearized about the centre. Integrating along the length of fibre β and summing over all fibres β as designated in (A 3) gives

$$\boldsymbol{u}_\alpha\left(\boldsymbol{r}_\alpha+s_\alpha\boldsymbol{p}_\alpha\right) = \sum_{\beta\neq\alpha}^{N_0}\int_{-l/2}^{l/2}\left[\boldsymbol{J}\left(\boldsymbol{r}_\alpha+s_\alpha\boldsymbol{p}_\alpha-\boldsymbol{r}_\beta\right)+s_\beta\left.\frac{\partial\boldsymbol{J}}{\partial s_\beta}\right|_{\boldsymbol{r}_\alpha+s_\alpha\boldsymbol{p}_\alpha-\boldsymbol{r}_\beta}+\cdots\right]\cdot\boldsymbol{f}\left(s_\beta\right)\mathrm{d}s_\beta. \tag{A 7}$$

The second term in the expansion makes no contribution to $\boldsymbol{u}_\alpha(\boldsymbol{r}_\alpha+s_\alpha\boldsymbol{p}_\alpha)$ and higher-order terms are ignored. Consequently, (A 7) becomes

$$\boldsymbol{u}_\alpha\left(\boldsymbol{r}_\alpha+s_\alpha\boldsymbol{p}_\alpha\right) \approx \sum_{\beta\neq\alpha}^{N_0}\boldsymbol{J}\left(\boldsymbol{r}_\alpha+s_\alpha\boldsymbol{p}_\alpha-\boldsymbol{r}_\beta\right)\cdot F\boldsymbol{e}_z, \tag{A 8}$$

where the approximation removes the dependence of the velocity on fibre α upon the orientation of fibre β. Substituting this approximation into (A 5) with $s_\alpha=0$ results in (2.1)–(2.3). Substituting (A 8) into (A 6) to calculate the rotational velocity within the approximation gives

$$\dot{\boldsymbol{p}}_\alpha = \left(\boldsymbol{I}-\boldsymbol{p}_\alpha\boldsymbol{p}_\alpha\right)\cdot\left.\frac{\partial\boldsymbol{J}}{\partial s_\alpha}\right|_{\boldsymbol{r}_\alpha-\boldsymbol{r}_\beta}\cdot F\boldsymbol{e}_z. \tag{A 9}$$

Calculating the gradient of the Oseen–Burger tensor and evaluating at $\boldsymbol{r}=\boldsymbol{r}_\alpha-\boldsymbol{r}_\beta$ gives

$$\left.\frac{\partial\boldsymbol{J}}{\partial s_\alpha}\right|_{\boldsymbol{r}} = \frac{1}{8\pi\mu}\left[\frac{\left(\boldsymbol{r}\cdot\boldsymbol{p}_\alpha\right)\boldsymbol{I}-\boldsymbol{p}_\alpha\boldsymbol{r}-\boldsymbol{r}\boldsymbol{p}_\alpha}{|\boldsymbol{r}|^3}+\frac{3\left(\boldsymbol{r}\cdot\boldsymbol{p}_\alpha\right)\boldsymbol{r}\boldsymbol{r}}{|\boldsymbol{r}|^5}\right], \tag{A 10}$$

where $|\boldsymbol{r}|$ is the distance between centres. Placing this relation in (A 9) gives (2.4), the rotational velocities for the fibres as used for the ‘fiblet’ simulations.

REFERENCES

Adachi, K., Kiriyama, S. & Koshioka, N. 1978 The behaviour of a swarm of particles moving in a viscous fluid. *Chem. Engng Sci.* **33**, 115–121.

Batchelor, G. K. 1970 Slender-body theory for particles of arbitrary cross-section in Stokes flow. *J. Fluid Mech.* **44**, 419–440.

Bosse, T., Kleiser, L., Härtel, C. & Meiburg, E. 2005 Numerical simulation of finite Reynolds number suspension drops settling under gravity. *Phys. Fluids* **17**, 037101.

Butler, J. E. & Shaqfeh, E. S. G. 2002 Dynamic simulations of the inhomogeneous sedimentation of rigid fibres. *J. Fluid Mech.* **468**, 205–237.

Cox, R. G. 1970 The motion of long slender bodies in a viscous fluid. Part 1. General theory. *J. Fluid Mech.* **44**, 791–810.

Ekiel-Jeżewska, M. L., Metzger, B. & Guazzelli, É. 2006 Spherical cloud of point particles falling in a viscous fluid. *Phys. Fluids* **18**, 038104.

Harlen, O. G., Sundararajakumar, R. R. & Koch, D. L. 1999 Numerical simulation of a sphere settling through a suspension of neutrally buoyant fibres. *J. Fluid Mech.* **388**, 355–388.

HASIMOTO, H. 1959 On the periodic fundamental solutions of the Stokes equations and their application to viscous flow past a cubic array of spheres. *J. Fluid Mech.* **5**, 317–328.

JEFFERY, G. B. 1922 The motion of ellipsoidal particles immersed in a viscous fluid. *Proc. R. Soc. Lond.* A **102**, 161–179.

MACHU, G., MEILE, W., NITSCHE, L. C. & SCHAFLINGER, U. 2001 Coalescence, torus formation and breakup of sedimenting drops: Experiments and computer simulations. *J. Fluid Mech.* **447**, 299–336.

MACKAPLOW, M. B. & SHAQFEH, E. S. G. 1998 A numerical study of the sedimentation of fibre suspensions. *J. Fluid Mech.* **376**, 149–182.

METZGER, B., NICOLAS, M. & GUAZZELLI, É. 2007 Falling clouds of particles in viscous fluids. *J. Fluid Mech.* **580**, 283–301.

MORAN, J. P. 1963 Line source distributions and slender-body theory. *J. Fluid Mech.* **17**, 285–304.

NITSCHE, J. M. & BATCHELOR, G. K. 1997 Breakup of a falling drop containing dispersed particles. *J. Fluid Mech.* **340**, 161–175.

PRESS, W. H., TEUKOLSKY, S. A., VETTERLING, W. T., & FLANNERY, B. P. 1994 *Numerical Recipes in Fortran, The Art of Scientific Computing*. 2nd edn., pp. 719–725. Cambridge University Press.

SAINTILLAN, D., SHAQFEH, E. S. G. & DARVE, E. 2006 The growth of concentration fluctuations in dilute dispersions of orientable and deformable particles under sedimentation. *J. Fluid Mech.* **553**, 347–388.

SCHAFLINGER, U. & MACHU, G. 1999 Interfacial phenomena in suspensions. *Chem. Engng Technol.* **22**, 617–619.